UNIVERSITY OF SÃO PAULO (USP)
SÃO CARLOS SCHOOL OF ENGINEERING (EESC)
AERONAUTICAL ENGINEERING DEPARTMENT (SAA)

Eduardo S. Larrubia

EFFECTS OF A PASSIVE PIEZOELECTRIC ABSORBER ON THE AEROELASTIC BEHAVIOR OF A THIN PLATE

São Carlos
2025

Eduardo S. Larrubia

EFFECTS OF A PASSIVE PIEZOELECTRIC ABSORBER ON THE AEROELASTIC BEHAVIOR OF A THIN PLATE

Monograph presented to the Aeronautical Engineering Program at the School of Engineering of São Carlos, University of São Paulo, as part of the requirements for obtaining the degree of Aeronautical Engineer.

Advisor: Prof. Dr. Carlos De Marqui Jr

São Carlos
2025

Ficha catalográfica elaborada pela Biblioteca “Prof. Dr. Sérgio Rodrigues Fontes” da EESC/USP com os dados inseridos pelo(a) autor(a)

L334e

Larrubia, Eduardo S.
Effects of a passive piezoelectric absorber on the aeroelastic behavior of a thin plate / Eduardo S. Larrubia; orientador Carlos De Marqui Junior. São Carlos, 2025.

Monografia (Graduação em Engenharia Aeronáutica) -- Escola de Engenharia de São Carlos da Universidade de São Paulo, 2025.

1. Aeroelasticity. 2. Piezoelectricity. 3. Flutter control. 4. Passive damping. 5. Supersonic flow. 6. Finite element method. I. Título.

Elaborado por Eduardo Graziosi Silva - CRB-8/8907

FOLHA DE APROVAÇÃO
Approval sheet

Candidato / *Student*: Eduardo Silveira Larrubia	
Título do TCC / *Title* **:** Effects of a passive piezoelectric absorber on the aeroelastic behavior of a thin plate	
Data de defesa / *Date*: 04/07/2025	

Comissão Julgadora / *Examining committee*	**Resultado** / *result*
Professor Titular Carlos De Marqui Junior	Aprovado
Instituição / Affiliation: EESC - SAA	
Doutora Larissa Drews Wayhs Lopes	APROVADO
Instituição / Affiliation: EESC **-** SAA	
Professor Doutor Ricardo Afonso Angélico	Aprovado
Instituição / Affiliation: EESC - SAA	

Presidente da Banca / Chair of the Examining Committee:

Professor Titular Carlos De Marqui Junior
(assinatura / *signature*)

Acknowledgments

First and foremost, I would like to express my deepest gratitude to my parents, Wiliam and Fabiana, and to my sisters, Ana Beatriz and Ana Luiza. Their unwavering support throughout every stage of my life, and their steadfast belief in education as an irreplaceable path for personal and professional growth, have been the foundation of my journey. I sincerely hope to honor the immense effort they made to ensure I had access to quality education. It is the greatest honor of my life to dedicate the conclusion of this academic chapter to them.

I am also deeply thankful to my girlfriend, Natalia, who has been a constant source of motivation and strength over the past year. Her support during each challenge and her inspiring dedication have helped me persevere and grow.

I would like to sincerely thank Prof. Dr. Carlos De Marqui Junior for his guidance and support. His aeroelasticity course revealed to me the beauty of aeronautical engineering, a field that elegantly unites structures, control, and aerodynamics—the very pillars of this program.

My heartfelt thanks also go to Prof. Dr. Larissa Drews Wayhs Lopes, whose constant assistance was vital to the development of this work. Her academic excellence is matched by an outstanding teaching ability and a natural talent for education. The Aeronautical Engineering Department at EESC is truly fortunate to have her, and I only regret not having had more opportunities to attend her classes.

I am profoundly grateful to Prof. Dr. Fernando Martini Catalano and Prof. Dr. Ricardo Afonso Angélico. Their mentorship went beyond the classroom—they were instrumental in every academic and professional project I participated in. I will always hold deep gratitude for them.

Finally, I would like to extend my sincere appreciation to Prof. Dr. Mr. Christophe Cuvier, Mr. Antony Costes, Mr. Diego Sodré, and Mr. Rafael Lima. I am incredibly thankful for the professional opportunities they provided me. Any academic or professional achievement I attain will always carry part of their contribution.

Abstract

The objective of this work is to study the application of piezoelectric materials in aerospace structures. Using the software developed by Wayhs-Lopes, L.D., this analysis is based on an electro-mechanically coupled plate configuration, exploring the properties of such materials, their integration into finite element models, the implementation of supersonic aerodynamic loading based on the Piston Theory, and the simulation of the coupled piezoaeroelastic system. The study aims to analyze the aeroelastic evolution and flutter boundary, seeking to increase the flutter speed through the use of piezoelectric materials. The expected outcome is an enhanced flutter tolerance and improved aeroelastic stability through passive control strategy.

Keywords: Piezoelectricity; Aeroelasticity; Piston theory; Supersonic flow; Finite element method; Flutter control; Passive damping;

Table of Contents

List of Figures

List of Tables

List of Symbols

L	Plate length
w	Plate width
h_s	Substrate thickness
h_p	Piezoelectric layer thickness
Y_s	Young's modulus of the substrate
ν_s	Poisson's ratio of the substrate
ρ_s	Density of the substrate
d_{31}	Piezoelectric strain coefficient
s_{11}^E	Elastic compliance at constant electric field
ε_{33}^T	Dielectric permittivity at constant stress
ε_0	Permittivity of vacuum
C_p	Capacitance of the piezoelectric layer
R	Shunt resistance
L_e	Shunt inductance
ω	Angular frequency
λ	Eigenvalue of the system
$\mathbf{K}$	Global stiffness matrix
$\mathbf{M}$	Global mass matrix
$\mathbf{C}$	Global damping matrix
$\mathbf{G}$	Aerodynamic stiffness matrix (piston theory)
$\boldsymbol{\psi}$	Mechanical degrees of freedom vector
$\boldsymbol{\phi}$	Mode shape (eigenvector)
$\mathbf{A}$	State-space matrix
$\mathbf{B}$	Input matrix for electrical coupling
$\mathbf{E}$	Electrical impedance matrix
M	Mach number
U_∞	Freestream velocity
ρ_∞	Freestream air density
b	Half-chord (piston theory reference)
p	Aerodynamic pressure
$\mathcal{L}$	Lagrangian of the system
$\mathcal{H}$	Hamiltonian functional
t	Time
x, y	In-plane spatial coordinates
$w(x, y, t)$	Transverse displacement of the plate

1 INTRODUCTION

1.1 Contextualization

Aeroelastic phenomena in high-speed flight, particularly under supersonic conditions, play a critical role in the design and operational safety of aerospace structures. Dynamic instabilities such as flutter can emerge, causing rapid structural failure and posing serious risks to control surfaces of supersonic aircraft, missile fins, and other lifting components. Therefore, flutter often imposes limits on the operational flight envelope, restricting speed, altitude, and maneuverability.

To analyze such phenomena, high-fidelity aeroelastic simulations combining CFD (Computational Fluid Dynamics) offer detailed insights but are often too computationally expensive for early-stage design or parametric investigations. Simplified quasi-static aerodynamic models like piston theory enable efficient approximation of supersonic aerodynamic loads and integrate naturally into finite-element formulations of thin plates.

At the same time, piezoelectric materials can provide passive and/or active vibration-control strategies for aeroelastic systems. Furthermore, they can provide energy harvesting by converting mechanical strain into electrical energy, which is attractive for power-limited platforms such as UAVs and guided munitions, but will not be discussed here. Embedding shunted piezoelectric layers into a thin-plate structure creates a coupled piezoaeroelastic system capable of dissipating vibrational energy and possibly raising the flutter speed, thereby extending operational life.

1.2 Objectives and work scope

This work studies the properties of piezoelectric materials and a simplified coupling of aerodynamic, elastic, and electrical domains—accounting for shunt impedance—to track aeroelastic evolution and the flutter boundary, aiming to increase flutter speed. It adapts the Python-based finite-element code developed by Wayhs-Lopes, L. D., which models a Kirchhoff thin plate with piston-theory aerodynamics, to evaluate flutter mitigation under supersonic flow.

2 MATHEMATICAL AND THEORY FRAMEWORK

Initially, it is important to define what are smart materials and, more specifically, piezoelectric effect and its general properties. Throughout this document, Voigt notation will be used for tensor representation.

2.1 Smart Materials and the Piezoelectric Effect

Smart materials are characterized by their ability to convert energy between different physical domains—mechanical, electrical, thermal, among others—through intrinsic coupling mechanisms. [3, 9]

These materials respond to external stimuli such as mechanical stress, electric fields, or temperature variations, producing measurable changes in shape, voltage, or other physical properties, as shown in Figure [1] provided by *Leo, D.J. (2007)* [10].

Figure 1 – Visual representation of coupling between physical domains

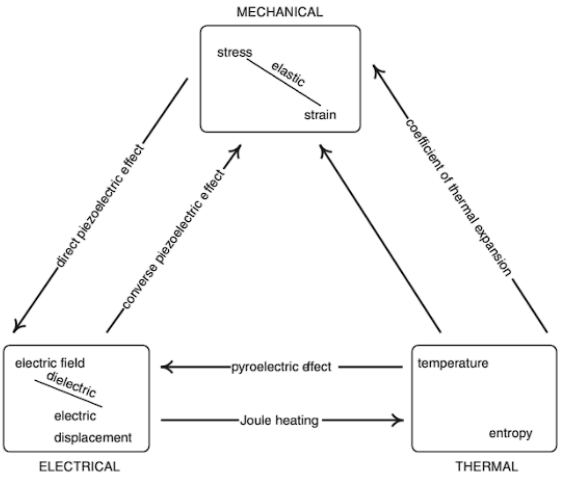

Fonte: Leo, D.J. (2007) [10]

Among the various types, piezoelectric materials are a well-established class of smart materials that exhibit electromechanical coupling: they generate electrical charge when mechanically deformed (direct effect) and undergo mechanical strain when subjected to an electric field (converse effect).

This bidirectional energy conversion makes piezoelectric materials particularly useful in applications such as sensors, actuators, vibration control, and energy harvesting [15] [6]. Their behavior is governed by a set of coupled constitutive equations linking mechanical stress and strain to electrical field and displacement which are going to be discussed in the next subsection.

2.1.1 Direct piezoelectric effect

When a linear elastic material is subjected to mechanical stress, the linear stress–strain relationship is given by:

$$S = sT \tag{2.1}$$

where S is the mechanical strain, T is the applied stress, and s is the mechanical compliance (the inverse of Young's modulus, Y). Unlike ordinary materials, however, piezoelectrics also generate an electric displacement coupled to mechanical loading, a phenomenon known as the *direct piezoelectric effect*. This effect is governed, in the linear range, by:

$$D = dT \tag{2.2}$$

where D is the electric displacement [C/m^2], and d is the piezoelectric strain coefficient [C/N]. The applied stress reorients internal electric dipoles, producing a measurable charge on electrodes attached to the material.

2.1.2 Converse piezoelectric effect

The piezoelectric materials also exhibit the *converse piezoelectric effect*, where an applied electric field induces mechanical strain.

Consider a piezoelectric material subjected to a constant voltage across its electrodes. Assuming the material behaves as a perfect insulator, the applied voltage generates an electric field E [V/m], which reorients the internal electric dipoles. At low field levels, the resulting electric displacement D is linearly related to the electric field by:

$$D = \varepsilon E \tag{2.3}$$

where ε is the dielectric permittivity of the material [F/m]. Beyond a certain field strength, this relationship becomes nonlinear due to dipole saturation.

More importantly, the electric field also induces mechanical deformation. In the linear regime, the induced strain S is proportional to the applied electric field:

$$S = dE \tag{2.4}$$

here, d is again the piezoelectric strain coefficient, now with units of m/V.

Therefore, we can rewrite the equations discussed before using a matrix notation to provide the linear constitutive piezoelectric equations,:

$$\begin{bmatrix} S \\ D \end{bmatrix} = \begin{bmatrix} s & d \\ d & \varepsilon \end{bmatrix} \begin{bmatrix} T \\ E \end{bmatrix} \tag{2.5}$$

The diagonal terms (s and ε) correspond to purely elastic and purely dielectric behavior, while the off-diagonal terms d quantify the strength of the piezoelectric coupling. The symmetry of the matrix reflects the reciprocity of the direct and converse effects.

2.1.3 Piezoelectric coupling coefficient

Equation (2.5) can be inverted to express stress and electric field as functions of strain and electric displacement:

$$\begin{bmatrix} T \\ E \end{bmatrix} = \frac{1}{s\varepsilon - d^2} \begin{bmatrix} \varepsilon & -d \\ -d & s \end{bmatrix} \begin{bmatrix} S \\ D \end{bmatrix} \tag{2.6}$$

Introducing the *piezoelectric coupling coefficient* k, defined as:

$$k = \frac{d}{\sqrt{s\varepsilon}}, \quad \text{with } 0 < k^2 < 1, \tag{2.7}$$

we can rewrite Equation (2.6) as:

$$\begin{bmatrix} T \\ E \end{bmatrix} = \frac{1}{1 - k^2} \begin{bmatrix} \frac{1}{s} & -\frac{k^2}{d} \\ -\frac{k^2}{d} & \frac{1}{\varepsilon} \end{bmatrix} \begin{bmatrix} S \\ D \end{bmatrix} \tag{2.8}$$

where the factor $1/(1 - k^2) > 1$ reflects the energy-conversion inefficiency inherent to piezoelectric transduction. The parameter k thus provides a normalized measure of electromechanical coupling efficiency, widely used for material comparison.

2.1.4 Boundary conditions

Due to electromechanical coupling, the effective material properties of piezoelectric devices depend on both mechanical and electrical boundary conditions.

Consider a piezoelectric material under mechanical stress T. If a *short-circuit* electrical boundary is applied ($E = 0$), the Equation (2.5) reduces to:

$$S = sT \tag{2.9}$$

$$D = dT \tag{2.10}$$

Now, under an *open-circuit* condition where no charge flow occurs ($D = 0$), using the inverse constitutive form, we get:

$$T = \frac{1}{s(1-k^2)} S \tag{2.11}$$

$$E = \frac{k^2}{d(1-k^2)} S \tag{2.12}$$

This shows that the mechanical compliance changes with the electrical boundary condition:

$$S = \begin{cases} sT & \text{(short-circuit)} \\ s(1-k^2)T & \text{(open-circuit)} \end{cases} \tag{2.13}$$

it follows that:

$$s^D = s^E(1-k^2) \tag{2.14}$$

where superscripts D and E denote constant electric displacement and constant electric field, respectively. This notation clarifies that mechanical compliance s is not intrinsic, but depends on the electrical boundary.

An analogous effect occurs for dielectric permittivity. Under mechanical boundary conditions, the permittivity changes:

$$\varepsilon^S = \varepsilon^T(1-k^2) \tag{2.15}$$

here, ε^S corresponds to a stress-free condition ($T = 0$), and ε^T to a strain-free (clamped, $S = 0$) condition.

Notably, the piezoelectric strain coefficient d is independent of boundary conditions.

2.1.5 Final constitutive notation

For our modeling, the stress tensor must be in the left side of the equation. Therefore, having in mind everything it was discussed until now, we can rewrite Equation (2.5) as:

$$\begin{bmatrix} \mathbf{T} \\ \mathbf{D} \end{bmatrix} = \begin{bmatrix} \mathbf{c}_p^E & -\mathbf{e}^t \\ \mathbf{e} & \boldsymbol{\varepsilon}^S \end{bmatrix} \begin{bmatrix} \mathbf{S} \\ \mathbf{E} \end{bmatrix} \tag{2.16}$$

Where:

- **T**: stress tensor
- **D**: electric displacement tensor
- **S**: strain tensor
- **E**: electric field tensor

- c^E: matrix of elastic stiffness under constant electric field
- $\mathbf{e}$: matrix of piezoelectric constraints (coupling factor)
- ε^S: matrix of electric permittivity under a stress-free condition

It is also important to take into account that, for our model, we are using piezoelectric constraints for a "closed circuit", as it will become clear in the modeling of our final system.

To better understand the mathematical modeling behind the final system, it is also important to understand the Kirchhoff's model for a thin plate.

2.2 Kirchhoff's model

Kirchhoff-Love plate theory, also known as Classical Plate Theory, is a fundamental model for the analysis of thin plates subjected to transverse loads. In the context of an aeroelastic electromechanical model, such as the one being developed in your work, understanding this theory is crucial for describing the structural behavior of both the host plate and the piezoelectric layers.

2.2.1 Fundamental Hypotheses of Kirchhoff-Love Theory

According to Reddy [16], the formulation of the structural model based on Kirchhoff-Love plate theory relies on three main hypotheses:

1. **Transverse Normals Remain Straight and Do Not Experience Elongation:** Straight lines that are perpendicular to the mid-surface of the plate before deformation remain straight and do not undergo elongation after deformation. This implies that the strain in the thickness direction ($S_3 = \frac{\partial w}{\partial z}$) is zero.
2. **Transverse Shear Strains are Neglected:** Transverse shear strains are considered negligible. This means that $S_4 = \frac{\partial v}{\partial z} + \frac{\partial w}{\partial y} = 0$ and $S_5 = \frac{\partial u}{\partial z} + \frac{\partial w}{\partial x} = 0$.
3. **In-Plane Displacements Vary Linearly with the Thickness Coordinate:** The in-plane dis- placements (u and v) vary linearly with the thickness coordinate z and are assumed to be due to bending only ($u = \frac{\partial u}{\partial z} z$ and $v = \frac{\partial v}{\partial z} z$).

These hypotheses allow the degrees of freedom to be expressed as functions of the independent transverse displacement w and its spatial derivatives ($\frac{\partial w}{\partial x}$ and $\frac{\partial w}{\partial y}$). Specifically, the displacement in the z-direction (w) is the only independent variable remaining in Hamilton's equation that will be presented in the next subsections of this documents.

So, having understood how the degrees of freedom should be written, let's move on to the 2D finite element model.

2.2.2 Finite Element Formulation for Thin Plate Modeling

To describe the mechanical behavior of the piezoelectric composite plate, a bi-dimensional finite element model is employed using rectangular four-node elements. Following what have been described in the last subsection and what was presented in the work of Wayhs-Lopes, L. D., we have that each node has three mechanical degrees of freedom: the transverse displacement w, and two bending rotations, and for each we have its correspondent strain tensor defined as:

$$\begin{gathered}\boldsymbol{u} = \left\{ \begin{array}{c} u \\ v \\ w \end{array} \right\} = \begin{bmatrix} -z & 0 & 0 \\ 0 & -z & 0 \\ 0 & 0 & 1 \end{bmatrix} \left\{ \begin{array}{c} \frac{\partial w}{\partial x} \\ \frac{\partial w}{\partial y} \\ w \end{array} \right\} = \mathbf{Z} \left\{ \begin{array}{c} \frac{\partial w}{\partial x} \\ \frac{\partial w}{\partial y} \\ w \end{array} \right\}, \\ \boldsymbol{S} = \left\{ \begin{array}{c} S_x \\ S_y \\ 2S_{xy} \end{array} \right\} = -z \left\{ \begin{array}{c} \frac{\partial^2 w}{\partial x^2} \\ \frac{\partial^2 w}{\partial y^2} \\ 2\frac{\partial^2 w}{\partial x \partial y} \end{array} \right\}. \end{gathered} \tag{2.17}$$

$$\theta_x = \frac{\partial w}{\partial y}, \quad \theta_y = \frac{\partial w}{\partial x} \tag{2.18}$$

Thus, each element has $4 \times 3 = 12$ degrees of freedom, which are collected in the elemental vector:

$$\boldsymbol{\psi} = \begin{bmatrix} w_1 \\ \theta_{x1} \\ \theta_{y1} \\ w_2 \\ \theta_{x2} \\ \theta_{y2} \\ w_3 \\ \theta_{x3} \\ \theta_{y3} \\ w_4 \\ \theta_{x4} \\ \theta_{y4} \end{bmatrix} \in \mathbb{R}^{12\times 1}$$

The continuous displacement field $w(x, y)$ is approximated within each element using a cubic polynomial in the local coordinates $r, s \in [-1, 1]$, centered at the element's geometric midpoint:

$$w(r, s) = \mathbf{p}^T(r, s)\, \mathbf{a}$$

where $\mathbf{a} \in \mathbb{R}^{12\times 1}$ is the vector of polynomial coefficients, and $\mathbf{p}(r, s)$ is the monomial vector:

$$\mathbf{p}(r,s) = \begin{bmatrix} 1 \\ r \\ s \\ r^2 \\ rs \\ s^2 \\ r^3 \\ r^2 s \\ rs^2 \\ s^3 \\ r^3 s \\ rs^3 \end{bmatrix}$$

The nodal values $(w_k, \theta_{xk}, \theta_{yk})$ at each node $k = 1, \ldots, 4$, which compose $\boldsymbol{\psi}$, are used to determine the coefficients $\mathbf{a}$. Since:

$$w(r_k, s_k) = p(r_k, s_k) \cdot a \Rightarrow a = p^{-1}(r_k, s_k) \cdot w(r_k, s_k) \tag{2.19}$$

Using the relations of the Equation [2.18], it is simple to arrive in the following equation:

$$w(r,s) = \Gamma(r,s) \cdot \psi, \Gamma = pP^{-1} \tag{2.20}$$

where $\mathbf{P} \in \mathbb{R}^{12\times12}$ is a constant matrix constructed by evaluating $\mathbf{p}$, $\partial\mathbf{p}/\partial r$, and $\partial\mathbf{p}/\partial s$ at the nodal coordinates (r_k, s_k).

The first derivatives with respect to global coordinates are given by:

$$\frac{\partial w}{\partial x} = \Gamma_x(r,s)\,\boldsymbol{\psi}, \quad \frac{\partial w}{\partial y} = \Gamma_y(r,s)\,\boldsymbol{\psi} \tag{2.21}$$

where:

$$\Gamma_x = \frac{\partial \mathbf{p}}{\partial r} \cdot \frac{2}{L_x} \cdot \mathbf{P}^{-1}, \quad \Gamma_y = \frac{\partial \mathbf{p}}{\partial s} \cdot \frac{2}{L_y} \cdot \mathbf{P}^{-1} \tag{2.22}$$

with L_x and L_y being the dimensions of the element in the x and y directions.

The full displacement vector $\mathbf{u}$ can be reconstructed under the Kirchhoff–Love assumptions using a transformation matrix $\mathbf{Z}$, leading to:

$$u = Z \begin{bmatrix} \Gamma_x \\ \Gamma_y \\ \Gamma \end{bmatrix} \psi = ZB_\eta\psi \tag{2.23}$$

Similarly, the strain field is given by:

$$S = \left\{ \begin{array}{c} S_x \\ S_y \\ 2S_{xy} \end{array} \right\} = -z \left\{ \begin{array}{c} \Gamma_{xx} \\ \Gamma_{yy} \\ 2\Gamma_{xy} \end{array} \right\} \psi = -zB_\kappa \psi \tag{2.24}$$

The second derivatives of $\mathbf{p}$ are computed as:

$$\frac{\partial^2 \mathbf{p}}{\partial x^2} = \frac{\partial^2 \mathbf{p}}{\partial r^2} \left(\frac{2}{L_x} \right)^2, \quad \frac{\partial^2 \mathbf{p}}{\partial y^2} = \frac{\partial^2 \mathbf{p}}{\partial s^2} \left(\frac{2}{L_y} \right)^2, \quad \frac{\partial^2 \mathbf{p}}{\partial x \partial y} = \frac{\partial^2 \mathbf{p}}{\partial r \partial s} \left(\frac{2}{L_x} \cdot \frac{2}{L_y} \right) \tag{2.25}$$

These expressions are used to build the strain–displacement matrix $\mathbf{B}_\kappa$, essential for assembling the stiffness matrix in the finite element formulation of the Kirchhoff plate.

In summary, we were able to write the displacement field u and the strain field S as function of w and the position on the plate (x, y).

Since the FEM is well described, the last missing part to understand the piezoaeroelastic model is the aerodynamic part: the Piston Theory.

2.3 Piston Theory for Supersonic Flow

Following the foundational work of Ashley and Zartarian [1], piston theory has been widely adopted as a simplified approach for modeling aerodynamic loading in supersonic regimes. It provides a first-order analytical model for estimating unsteady aerodynamic pressure on surfaces in supersonic flow. It assumes small disturbances propagating along streamlines and neglects effects such as flow separation, viscosity, and shock-boundary layer interaction. This theory is particularly suited for slender structures, such as panels or control surfaces, where detailed CFD simulations are impractical during early design stages.

Consider a panel undergoing out-of-plane deformation $w(x, t)$. The interaction between the surface and the surrounding supersonic flow induces a pressure perturbation Δp, which acts normal to the panel. The resultant aerodynamic force is obtained by integrating this pressure over the panel's surface A_{xy}:

$$F_{az} = \int_{A_{xy}} \Delta p(x, t)\, dA \tag{2.26}$$

In the classical first-order piston theory, the pressure difference is expressed as a linear combination of the local slope and velocity of the surface:

$$\Delta p(x, t) = -\left(\alpha \frac{\partial w}{\partial x} + \beta \frac{\partial w}{\partial t} \right) \tag{2.27}$$

where the aerodynamic coefficients are defined as:

$$\alpha = \frac{2q}{\sqrt{Ma^2 - 1}}, \tag{2.28}$$

$$\beta = \frac{2q}{V} \cdot \frac{Ma^2 + 2}{(Ma^2 - 1)^{3/2}}, \tag{2.29}$$

$$q = \frac{1}{2}\rho V^2 \tag{2.30}$$

Here, ρ is the air density, V is the freestream velocity, and Ma is the Mach number. The term $\partial w/\partial x$ accounts for compressive effects due to the surface slope, while $\partial w/\partial t$ reflects unsteady inertial loading. The negative sign indicates that the resulting aerodynamic force opposes the panel's motion.

Piston theory is valid for $Ma > 1$ and will be used in this piezoaeroelastic analyses, since it provides accurate trend predictions with significantly reduced computational effort.

With that we have all the information needed to conceive the elemental model for the system.

3 MODEL GOVERNING EQUATIONS

3.1 Governing Equations of a Single Finite Element

The formulation of the governing equations for a single element of an electromechanical aeroelastic plate is based on the generalized Hamilton's principle, which states that the time variation of the total Lagrangian (kinetic energy minus potential energy), plus the virtual work of non-conservative forces (aerodynamic and electrical), must be zero:

$$\int_{t_1}^{t_2} (\delta T - \delta U + \delta W_e + \delta W + \delta W_a)\, dt = 0 \tag{3.1}$$

Where:

- T is the total kinetic energy of the system, including the host structure and the piezoelectric layers;
- U is the total strain (elastic) energy stored in the host and piezoelectric materials;
- W_e is the electrical energy stored in the piezoelectric layers due to the electric field;
- W is the external work done by non-conservative mechanical forces and electric charges extracted from the system and it is related to the circuit connected to the plates;
- W_a is the work done by aerodynamic forces on the plate surface;
- δ indicates the first variation with respect to the virtual displacements and electric potential.

The terms are defined as:

$$T = \int_{V_s} \frac{1}{2}\rho_s \dot{\mathbf{u}}^T \dot{\mathbf{u}}\, dV_s + \int_{V_p} \frac{1}{2}\rho_p \dot{\mathbf{u}}^T \dot{\mathbf{u}}\, dV_p \tag{3.2}$$

$$U = \int_{V_s} \frac{1}{2}\mathbf{S}^T \mathbf{T}_s\, dV_s + \int_{V_p} \frac{1}{2}\mathbf{S}^T \mathbf{T}_p\, dV_p \tag{3.3}$$

$$W_e = \int_{V_p} \frac{1}{2}\mathbf{E}^T \mathbf{D}\, dV_p \tag{3.4}$$

$$\delta W = \delta v_p Q \tag{3.5}$$

$$\Delta p(w) = -\left(\alpha \frac{\partial w}{\partial x} + \beta \frac{\partial w}{\partial t}\right) \tag{3.6}$$

where:

- ρ_s, ρ_p are the densities of the substrate and piezoelectric layers, respectively;
- $\mathbf{u}$ is the displacement vector;
- $\mathbf{S}$ is the strain vector; $\mathbf{T}_s$, $\mathbf{T}_p$ are the stress vectors in the substrate and piezoelectric layers;
- $\mathbf{E}$ is the electric field vector; $\mathbf{D}$ is the electric displacement vector;
- v_p is the electrical potential across the piezoelectric layer;
- Q is the charge extracted from the element and passed to the external circuit;
- Δp is the aerodynamic pressure variation due to supersonic flow;
- w is the transverse displacement of the plate;
- α, $\beta =$ are piston theory coefficients presented before.

To define the system matrices, it is necessary to identify all physical contributions associated with the mechanical displacement vector $\boldsymbol{\psi}$, its first and second derivatives, and the electric potential v_p.

Structural Matrices

The mass and stiffness matrices account for the mechanical behavior of both the host structure and the piezoelectric layers:

$$\mathbf{m} = \int_{V_s} \mathbf{B}_\eta^T \mathbf{Z}^T \rho_s \mathbf{Z} \mathbf{B}_\eta \, dV_s + \int_{V_p} \mathbf{B}_\eta^T \mathbf{Z}^T \rho_p \mathbf{Z} \mathbf{B}_\eta \, dV_p \tag{3.7}$$

$$\mathbf{k} = \int_{V_s} z^2 \mathbf{B}_\kappa^T \overline{\mathbf{c}}_s \mathbf{B}_\kappa \, dV_s + \int_{V_p} z^2 \mathbf{B}_\kappa^T \overline{\mathbf{c}}_p^E \mathbf{B}_\kappa \, dV_p \tag{3.8}$$

The matrix $\mathbf{m}$ captures inertial effects from both the base plate (subscript s) and the piezoelectric layers (subscript p), where ρ denotes density and $\mathbf{Z}$ is the transformation matrix linking displacements to the mid-surface. The stiffness matrix $\mathbf{k}$ includes bending rigidity contributions, weighted by z^2, consistent with Kirchhoff plate theory, and depends on the material stiffness tensors $\overline{\mathbf{c}}_s$ and $\overline{\mathbf{c}}_p^E$ for the elastic and piezoelectric layers, respectively.

Aerodynamic Matrices

Aerodynamic effects are incorporated via additional stiffness and damping-like matrices, derived from piston theory for supersonic flows:

$$\mathbf{k}_a = -\alpha \int_{A_{xy}} \boldsymbol{\Gamma}^T \boldsymbol{\Gamma}_x \, dA \tag{3.9}$$

$$\mathbf{c}_a = -\beta \int_{A_{xy}} \boldsymbol{\Gamma}^T \boldsymbol{\Gamma} \, dA \tag{3.10}$$

here, α and β are aerodynamic coefficients that depend on the freestream conditions (Mach number, density, and velocity), while $\boldsymbol{\Gamma}$ and its derivatives represent the shape functions used to describe transverse displacement within the element. The matrix $\mathbf{k}_a$ contributes to the aerodynamic stiffness, and $\mathbf{c}_a$ to the aerodynamic damping — both critical for capturing flutter behavior.

Electromechanical Coupling

The coupling between mechanical and electrical domains due to the piezoelectric effect is captured by the vector $\boldsymbol{\theta}_p$:

$$\boldsymbol{\theta}_p = \int_{V_p} z \mathbf{B}_\kappa^T \bar{\mathbf{e}}^T B_E \, dV_p \tag{3.11}$$

This term links structural deformation to electric charge generation (direct effect), and conversely, the application of voltage to induced mechanical strain (inverse effect). The piezoelectric constant matrix $\bar{\mathbf{e}}$ is coupling factor presented before.

Electrical Capacitance

Finally, the capacitance associated with the piezoelectric layers is given by:

$$C_p = \int_{V_p} B_E^T \bar{\boldsymbol{\epsilon}}^S B_E \, dV_p \tag{3.12}$$

This scalar represents the electrical energy storage capacity of the piezoelectric material, where $\bar{\boldsymbol{\epsilon}}^S$ is the permittivity matrix under constant strain. It directly influences the charge-voltage dynamics of the system and plays a central role when external electrical circuits (e.g., shunt networks) are introduced.

Together, these element-level matrices define the dynamic behavior of the coupled piezoaeroelastic system. In the next section, they will be assembled into global matrices to form the full system of equations governing the time evolution and stability of the structure under supersonic flow.

By applying the calculus of variations and separating the contributions of the mechanical degrees of freedom $\boldsymbol{\psi}$ and the electrical degree of freedom v_p, we obtain the coupled equations of motion for a single element:

$$\mathbf{m}\ddot{\boldsymbol{\psi}} + \mathbf{c}_a\dot{\boldsymbol{\psi}} + (\mathbf{k} + \mathbf{k}_a)\boldsymbol{\psi} - \boldsymbol{\theta} v_p = \mathbf{f} \tag{3.13}$$

$$C_p \dot{v}_p + \frac{1}{Z_{eq}} v_p + \boldsymbol{\theta}^T \dot{\boldsymbol{\psi}} = 0 \tag{3.14}$$

where:

- $\boldsymbol{\psi} \in \mathbb{R}^{12\times 1}$ is the vector of nodal mechanical degrees of freedom: vertical displacement w and slopes θ_x, θ_y at each of the four nodes.
- v_p is the electrical potential difference across the piezoelectric layer.
- $\mathbf{m}$ and $\mathbf{k}$ are the elemental structural mass and stiffness matrices.
- $\mathbf{c}_a$ and $\mathbf{k}_a$ are the aerodynamic damping and stiffness matrices from piston theory.
- $\boldsymbol{\theta}$ is the electromechanical coupling vector.
- C_p is the capacitance of the element.
- Z_{eq} is the equivalent shunt impedance of the external circuit.

Therefore, the formulation of the finite element model enables the definition of the system matrices at the element level, capturing the contributions from mechanical inertia, stiffness, aerodynamic loading, piezoelectric coupling, and electrical storage. These matrices form the foundation of the coupled electromechanical system.

3.2 Final Model: Global Equations

Once the element-level formulations are established, the standard finite element assembly procedure is applied to construct the global system of equations governing the aeroelastic electromechanical behavior of the structure.

In the most general formulation, each finite element is initially considered to possess its own independent electrical degree of freedom, corresponding to the voltage v_p across its piezoelectric layer. This leads to the construction of a global capacitance matrix $\mathbf{C}_p \in \mathbb{R}^{n_e \times n_e}$, and a global electromechanical coupling matrix $\boldsymbol{\Theta} \in \mathbb{R}^{n_m \times n_e}$, where n_e is the number of elements and n_m the total number of mechanical degrees of freedom.

However, in practice, the electrodes bracketing the piezoelectric layers are highly conductive, allowing groups of elements to be electrically connected through a shared electrode region. Each of these regions is wired to a single external shunt circuit, and thus responds with a common voltage output v_i. If we define n_r as the number of such electrode regions, the electrical problem is greatly reduced in size and complexity.

The electrical assembly then proceeds as follows:

- The total capacitance $C_{p,ii}$ of region i is obtained by summing the capacitances of all elements it contains.

- The i-th column of the global coupling matrix $\boldsymbol{\Theta}$ is constructed by summing the electromechanical coupling vectors of all elements belonging to region i.

The reduced system involves the following quantities:

- $\mathbf{M}, \mathbf{K} \in \mathbb{R}^{n_m \times n_m}$: global structural mass and stiffness matrices;
- $\mathbf{C}_a, \mathbf{K}_a \in \mathbb{R}^{n_m \times n_m}$: global aerodynamic damping and stiffness matrices, derived from piston theory;
- $\boldsymbol{\Theta} \in \mathbb{R}^{n_m \times n_r}$: global electromechanical coupling matrix;
- $\mathbf{C}_p \in \mathbb{R}^{n_r \times n_r}$: global capacitance matrix for the electrode regions;
- $\mathbf{v} \in \mathbb{R}^{n_r \times 1}$: vector of voltages from each region;
- $\boldsymbol{\psi} \in \mathbb{R}^{n_m \times 1}$: vector of mechanical degrees of freedom;
- $\mathbf{F} \in \mathbb{R}^{n_m \times 1}$: external mechanical force vector (here assumed zero).

The coupled system of differential equations in the time domain can now be written as:

$$\begin{aligned} \mathbf{M}\ddot{\boldsymbol{\psi}} + \mathbf{C}_a\dot{\boldsymbol{\psi}} + (\mathbf{K} + \mathbf{K}_a)\boldsymbol{\psi} - \boldsymbol{\Theta}\mathbf{v} = \mathbf{F} \\ \mathbf{C}_p\dot{\mathbf{v}} + \mathbf{Z}_{\text{eq}}^{-1}\mathbf{v} + \boldsymbol{\Theta}^T\dot{\boldsymbol{\psi}} = \mathbf{0} \end{aligned} \tag{3.15}$$

The matrix $\mathbf{Z}_{\text{eq}}^{-1} \in \mathbb{C}^{n_r \times n_r}$ is the inverse of the equivalent impedance of the external shunt circuits, describing the electrical dynamics of the system. Assuming linear RLC components in each region, it takes the form:

$$\mathbf{Z}_{\text{eq}}^{-1} = \left(j\omega\mathbf{L} + \mathbf{R} + \frac{1}{j\omega\mathbf{C}_{\text{ext}}} \right)^{-1} \tag{3.16}$$

Here, $\mathbf{L}, \mathbf{R}, \mathbf{C}_{\text{ext}} \in \mathbb{R}^{n_r \times n_r}$ are diagonal matrices whose i-th diagonal entries correspond to the inductance, resistance, and external capacitance of the i-th shunt circuit. In this work, external capacitors are not considered, and thus $\mathbf{C}_{\text{ext}} = \mathbf{0}$.

To incorporate this impedance expression into the time-domain formulation, one applies the Laplace transform to the second Equation of [3.15], performs algebraic manipulation, and then returns to the time domain. This yields the final coupled system:

$$\begin{aligned} \mathbf{M}\ddot{\boldsymbol{\psi}} + \mathbf{C}_a\dot{\boldsymbol{\psi}} + (\mathbf{K} + \mathbf{K}_a)\boldsymbol{\psi} - \boldsymbol{\Theta}\mathbf{v} = \mathbf{0} \\ \mathbf{L}\boldsymbol{\Theta}^T\ddot{\boldsymbol{\psi}} + \mathbf{R}\boldsymbol{\Theta}^T\dot{\boldsymbol{\psi}} + \boldsymbol{C}^{-1}\boldsymbol{\Theta}^T\boldsymbol{\psi} + \mathbf{L}\mathbf{C}_p\ddot{\mathbf{v}} + \mathbf{R}\mathbf{C}_p\dot{\mathbf{v}} + (\mathbf{C}^{-1}\mathbf{C}_p + I)\mathbf{v} = \mathbf{0} \end{aligned} \tag{3.17}$$

This system represents the full coupling between the structural, aerodynamic, and electrical domains. The first equation governs the structural dynamics under the influence of both mechanical and electrical effects. The second equation captures the electrical response induced by mechanical deformation and describes how energy is dissipated or harvested via external electrical circuits.

This aspect is central to the current work: by converting mechanical energy into electrical energy, which is then dissipated in the shunt circuits, the piezoelectric layers function as passive vibration absorbers. This energy dissipation mechanism is expected to attenuate aeroelastic responses, such as flutter, and thus enhance the structural stability under supersonic flow conditions.

4 MODAL ANALYSIS - EIGENVECTOR PROBLEM

The idea is to translate the model explained before into a structured code in order to test the hypothesis of structural stability increase due to the energy harvest system.

First of all, we can rewrite the Equation (3.17) in a matrix form:

$$\begin{bmatrix} \mathbf{M} & \mathbf{0} \\ \mathbf{L}\boldsymbol{\Theta}^T & \mathbf{L}\mathbf{C}_p \end{bmatrix} \begin{bmatrix} \ddot{\boldsymbol{\psi}} \\ \ddot{\mathbf{v}} \end{bmatrix} + \begin{bmatrix} \mathbf{C}_a & \mathbf{0} \\ \mathbf{R}\boldsymbol{\Theta}^T & \mathbf{R}\mathbf{C}_p \end{bmatrix} \begin{bmatrix} \dot{\boldsymbol{\psi}} \\ \dot{\mathbf{v}} \end{bmatrix} + \begin{bmatrix} \mathbf{K} + \mathbf{K}_a & -\boldsymbol{\Theta} \\ C^{-1}\boldsymbol{\Theta}^T & C^{-1}\mathbf{C}_p + I \end{bmatrix} \begin{bmatrix} \boldsymbol{\psi} \\ \mathbf{v} \end{bmatrix} = \mathbf{0} \tag{4.1}$$

With that in mind, we can create the variable u defined as:

$$\mathbf{u} = \begin{bmatrix} \boldsymbol{\psi} \\ \mathbf{v} \end{bmatrix} \tag{4.2}$$

Therefore, we can rewrite the system as follows:

$$\mathbf{A}\ddot{\mathbf{u}} + \mathbf{B}\dot{\mathbf{u}} + \mathbf{C}\mathbf{u} = \mathbf{0} \tag{4.3}$$

Where:

$$\mathbf{A} = \begin{bmatrix} \mathbf{M} & \mathbf{0} \\ \mathbf{L}\boldsymbol{\Theta}^T & \mathbf{L}\mathbf{C}_p \end{bmatrix}, \quad \mathbf{B} = \begin{bmatrix} \mathbf{C}_a & \mathbf{0} \\ \mathbf{R}\boldsymbol{\Theta}^T & \mathbf{R}\mathbf{C}_p \end{bmatrix}, \quad \mathbf{C} = \begin{bmatrix} \mathbf{K} + \mathbf{K}_a & -\boldsymbol{\Theta} \\ C^{-1}\boldsymbol{\Theta}^T & C^{-1}\mathbf{C}_p + I \end{bmatrix} \tag{4.4}$$

This modification is very appropriate since the differential Equation [4.3] has a very well known behavior and we can explore the solution using the state-space form.

We can also rewrite the previous equations as:

$$\begin{cases} \ddot{\mathbf{u}} = -\mathbf{A}^{-1}\mathbf{B}\dot{\mathbf{u}} - \mathbf{A}^{-1}\mathbf{C}\mathbf{u} \\ \dot{\mathbf{u}} = \dot{\mathbf{u}} \end{cases} \tag{4.5}$$

That being the case, we have to apply another transformation:

$$\mathbf{x} = \begin{bmatrix} \dot{\mathbf{u}} \\ \mathbf{u} \end{bmatrix} \tag{4.6}$$

where x will be the space-state variable.

So, using this change of variables, we have:

$$\dot{\mathbf{x}} = \begin{bmatrix} -\mathbf{A}^{-1}\mathbf{B} & -\mathbf{A}^{-1}\mathbf{C} \\ \mathbf{I} & \mathbf{0} \end{bmatrix} \mathbf{x} \tag{4.7}$$

This is a linear time-invariant system, therefore it can be analyzed by assuming solutions of exponential form, which is a classical approach in the study of linear differential equations. The solution is assumed to take the form:

$$\mathbf{x}(t) = \mathbf{X}e^{\lambda t} \tag{4.8}$$

where $\mathbf{X} \in \mathbb{C}^n$ is a constant vector representing the mode shape, and $\lambda \in \mathbb{C}$ is a scalar representing the exponential growth rate (or decay rate) and frequency.

Substituting Equation [4.8] into the differential equation:

$$\frac{d}{dt}\left(\mathbf{X}e^{\lambda t}\right) = \begin{bmatrix} -\mathbf{A}^{-1}\mathbf{B} & -\mathbf{A}^{-1}\mathbf{C} \\ \mathbf{I} & \mathbf{0} \end{bmatrix} \mathbf{X}e^{\lambda t} \tag{4.9}$$

Computing the derivative on the left-hand side leads to:

$$\lambda \mathbf{X}e^{\lambda t} = \begin{bmatrix} -\mathbf{A}^{-1}\mathbf{B} & -\mathbf{A}^{-1}\mathbf{C} \\ \mathbf{I} & \mathbf{0} \end{bmatrix} \mathbf{X}e^{\lambda t} \tag{4.10}$$

Since $e^{\lambda t} \neq 0$, it can be canceled from both sides of the equation, resulting in:

$$\lambda \mathbf{X} = \begin{bmatrix} -\mathbf{A}^{-1}\mathbf{B} & -\mathbf{A}^{-1}\mathbf{C} \\ \mathbf{I} & \mathbf{0} \end{bmatrix} \mathbf{X} \tag{4.11}$$

This is a standard **eigenvalue problem**, where the scalar λ is an eigenvalue and the vector $\mathbf{X}$ is the corresponding eigenvector of the system matrix. Solving this problem provides key insights into the system dynamics:

- If $\mathrm{Re}(\lambda) < 0$, the mode decays exponentially — indicating a stable response.
- If $\mathrm{Re}(\lambda) > 0$, the mode grows with time — leading to instability.
- If λ is purely imaginary, the mode corresponds to an undamped oscillation.

And that becomes clear as the definition of the damping factor is:

$$\zeta = \frac{-\mathrm{Re}(\lambda)}{|\lambda|} \tag{4.12}$$

So, if $\mathrm{Re}(\lambda) > 0$, then $\zeta < 0$, which implicates a unstable system. For our analysis, it is important to find the point where $\mathrm{Re}(\lambda)$ is zero. This condition, where the real part of the dominant eigenvalue crosses zero, marks a dynamic bifurcation: the onset of flutter. At this point, the system oscillates with no net energy loss or gain, corresponding to purely imaginary eigenvalues. The imaginary part of the critical eigenvalue defines the flutter frequency, expressed as

$$\omega_f = \mathrm{Im}(\lambda)$$

This frequency characterizes the structural oscillation at the onset of instability and serves as a fundamental reference in aeroelastic analyses. Consequently, identifying the vibration frequency associated with the dominant mode is essential, as it allows for the tuning of the electromechanical system to maximize damping at this critical condition. By aligning the control strategy with this frequency, it becomes possible to enhance energy dissipation and effectively delay the onset of divergent aeroelastic phenomena.

5 SHUNT CIRCUIT PARAMETERS

The model of this study has a resistive-inductive (RL) shunt circuit, which can be used to enhance the damping characteristics [20, 12].

Figure 2 – Plate model – Piezoelectric layer and shunt circuit

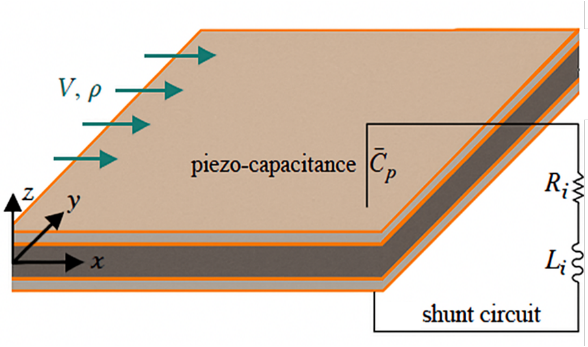

Source: Modified from Wayhs-Lopes, L.D.

To achieve optimal energy dissipation, the electrical parameters of the shunt must be carefully tuned to interact effectively with the mechanical dynamics of the structure. A fundamental strategy in this context is to tune the RL circuit to a desired mechanical frequency, typically the flutter frequency ω_f. This tuning is achieved by adjusting the inductance L_i and the resistance R_i, so that the natural (resonant) frequency of the electrical circuit matches the frequency of the aeroelastic phenomena.

From standard LC circuit theory, the tuning frequency ω_t is given by:

$$\omega_t = \frac{1}{\sqrt{L_i \bar{C}_p}}, \tag{5.1}$$

where L_i is the inductance and $\bar{C}_p$ is the equivalent capacitance of the electrode region, which may include multiple finite elements grouped under a single external circuit. This expression is derived from the governing equation:

$$L_i \ddot{q} + R_i \dot{q} + \frac{1}{\bar{C}_p} q = 0. \tag{5.2}$$

To introduce energy dissipation into the system, a resistor R_i is added in series with the inductor, forming a classical RLC series circuit. This configuration not only allows the circuit to be tuned to the structural vibration frequency, but also enables controlled dissipation of energy through electrical damping.

The damping behavior of such a circuit is governed by the damping ratio ζ, defined by the standard second-order system analogy:

$$\zeta = \frac{R_i}{2}\sqrt{\frac{\bar{C}_p}{L_i}}, \tag{5.3}$$

where $\bar{C}_p$ is the equivalent capacitance of the piezoelectric layers and L_i is the inductance in the shunt branch. Rearranging the equation allows one to compute the resistance necessary to achieve a target damping ratio ζ:

$$R_i = 2\zeta\sqrt{\frac{L_i}{\bar{C}_p}}. \tag{5.4}$$

This expression provides a useful reference when designing the shunt circuit, particularly in guiding the initial selection of electrical resistance. In principle, setting the tuning frequency ω_t equal to the dominant structural or aeroelastic frequency (e.g., the pre-flutter frequency ω_f) and selecting a target damping ratio ζ enables the computation of a corresponding resistance via Equation (5.4).

However, defining an appropriate value for ζ is not straightforward in coupled electromechanical systems. Unlike classical second-order oscillators, where ζ directly characterizes the system's transient response, here it pertains only to the electrical subdomain. The actual damping introduced into the global system depends on:

- the electromechanical coupling strength between the piezoelectric layers and the structure;
- the proximity between the electrical tuning frequency and the structural modes;
- and the spatial and modal distribution of the piezoelectric patches.

As such, the global damping behavior may not correlate directly with the nominal value of ζ, and its initial selection remains somewhat arbitrary. Iterative or parametric studies are typically necessary to identify effective configurations.

As discussed by Hagood and von Flotow [7], optimal power transfer occurs when the circuit is tuned to a modal frequency and the resistance is adjusted according to the piezoelectric coupling coefficient. Still, if the patches are poorly placed or the targeted mode exhibits low strain energy in their region, the resulting energy dissipation remains limited.

Therefore, while Equation (5.4) offers a valuable electrical design rule, the optimal configuration of R and L for suppressing aeroelastic instabilities must be determined based on the full electromechanical system response.

With these relations established, the next section applies the model and explores its results.

6 IMPLEMENTATION AND DISCUSSION OF RESULTS

6.1 Structural and Piezoelectric Properties

The structural and piezoelectric parameters considered in the model are summarized in Table 1.

A bimorph configuration (see Figure [2]) is adopted, with continuous piezoelectric layers symmetrically bonded to the upper and lower surfaces of the metallic substrate. Each piezoelectric patch has thickness $h_p = 1.0 \times 10^{-4}$ m, and the material employed is PZT-5A. The electrodes are assumed to be perfectly conductive and grouped uniformly across the domain. The upper and lower electrodes are connected in series and interface with an external RL shunt circuit.

The piezoelectric, dielectric, and elastic properties of PZT-5A are defined according to standardized values [7] and consistent with the values used by Wayhs-Lopes, L. D. In particular, the effective coupling coefficient used in the nondimensional analysis satisfies the relation $k = d/\sqrt{s\varepsilon}$, where d is the piezoelectric constant, s the compliance, and ε the dielectric permittivity.

Table 1 – Mechanical and piezoelectric properties of the substrate and PZT-5A piezoelectric layer

Property	**Value**
Plate length, L [m]	0.300
Plate width, w [m]	0.300
Substrate thickness, h_s [m]	1.0×10^{-3}
Piezo layer thickness, h_p [m]	1.0×10^{-4}
Young's modulus (substrate), Y_s [GPa]	210
Poisson's ratio (substrate), ν_s [-]	0.33
Density (substrate), ρ_s [kg/m^3]	7930
Piezoelectric coupling coeff., d_{31} [pC/N]	-190
Elastic compliance, s_{11}^E [m^2/N]	16.4×10^{-12}
Dielectric permittivity, $\varepsilon_{33}^T/\varepsilon_0$ [-]	1800

Source: Elaborated by the author.

A finite element mesh with 16×16 Kirchhoff plate elements is employed for all simulations. The electrode region is discretized identically, with electrical degrees of freedom concentrated in a single node group associated with the global capacitance matrix $\mathbf{C}_p$.

This setup allows consistent comparison between open-circuit and shunted configurations while preserving mechanical resolution.

6.2 Short-Circuit Conditions

In this configuration, the electrodes of the piezoelectric layers are connected through a vanishing impedance ($R = 0\ \Omega$, $L = 10^{-9}$ H), effectively imposing a short-circuit condition. This enforces $E = 0$, which, according to the constitutive relations discussed in Section 2.1.4, results in reduced stiffness of the piezoelectric material due to the absence of electric field counteraction.

Figures 3 and 4 show the evolution of the real and imaginary parts of the eigenvalues under short-circuit conditions, based on a mode-tracked analysis. As observed in Figure 3, flutter occurs at Ma = 3.066, where a complex-conjugate pair of eigenvalues crosses into the unstable region, indicated by a positive real part. As the numerical model is discretized, and flutter is theoretically defined at the point where the real part of the eigenvalue crosses zero, we adopt for simplicity the convention that the flutter speed corresponds to the first Mach number at which a mode exhibits a real part greater than or equal to zero. Therefore, the true flutter speed may be underestimated by up to one Mach step, in this case, 0.001.

Since the higher-order vibration modes demonstrated greater stability, for the sake of clarity, only the first four modes (i.e., the first eight eigenvalues) are shown in the plots.

Figure 3 – Real part of eigenvalues under short-circuit conditions with modal tracking

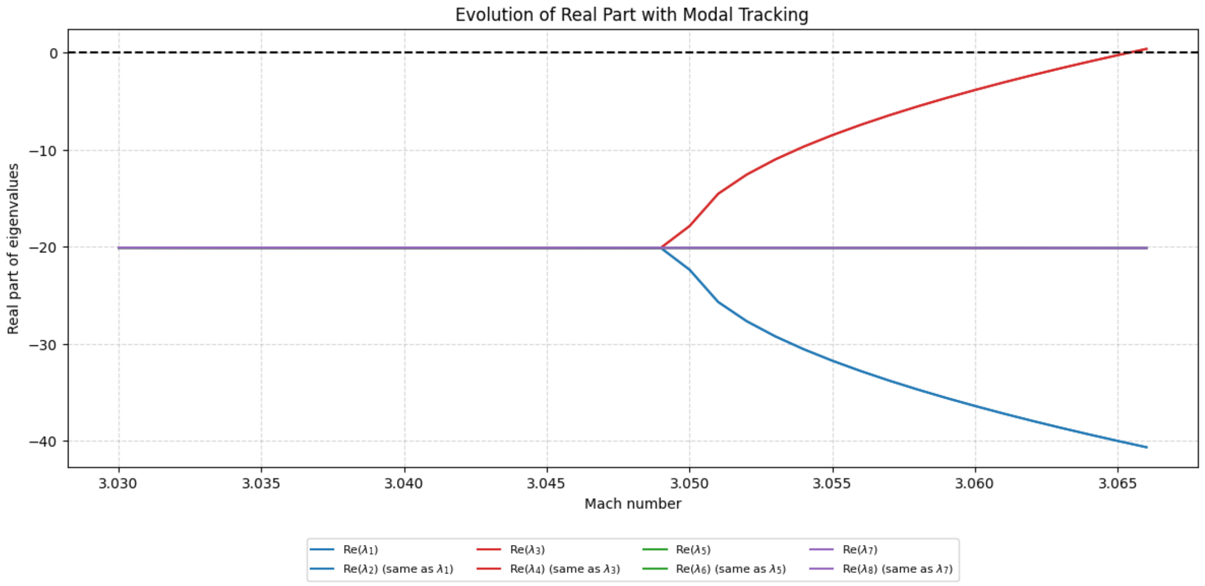

Source: Elaborated by the author.

The label ”same as λx”indicates that the corresponding mode follows a trajectory coincident with mode λx, based on a numerical similarity criterion. It is important to note that the complex conjugate of an eigenvalue is also an eigenvalue of the problem. Therefore, eigenvalues 1 and 2 correspond to vibration mode 1, eigenvalues 3 and 4 to mode 2, and so on. From Figure [3], we observe that the eigenvalues associated with the second vibration mode (λ_3 and λ_4) are the ones that become unstable as the Mach number increases and cross into the right-half complex plane.

The corresponding modal frequencies are shown in Figure [4].

Figure 4 – Modal frequencies under short-circuit conditions

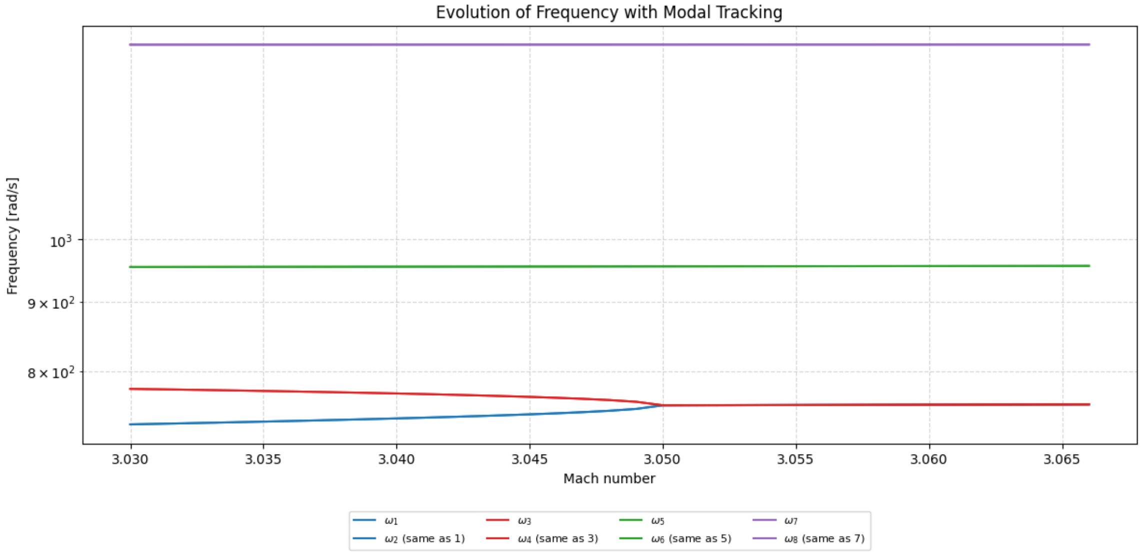

Source: Elaborated by the author.

It is evident from Figure 4 that coalescence between the first and second modes occurs at approximately Mach 3.049. In other words, the modal frequencies of the first and second modes approach each other and, in this particular case, merge, resulting in a frequency degeneracy where the two curves are no longer distinguishable. This phenomenon is a classical precursor to flutter onset, as the interaction and merging of modes lead to the destabilization observed in the real part of the eigenvalues.

Additionally, after the onset of flutter, the first mode retains a negative real part, indicating it remains stable, even though its frequency is nearly identical to that of the unstable mode at the flutter boundary. This highlights the importance of accurate modal identification.

The eigenvalues of the first four modes are represented in the complex plane in Figure [5]. This plot further confirms the flutter bifurcation mechanism: as the Mach number increases, a pair of eigenvalues migrates from the left-half to the right-half plane, resulting in the loss of system stability. The trajectory in the complex plane is typical of a classical flutter event, with the real part crossing zero and the imaginary part indicating the oscillatory character of the instability.

Figure 5 – First four modes of the system represented in the complex plane at the flutter Mach under short-circuit condition

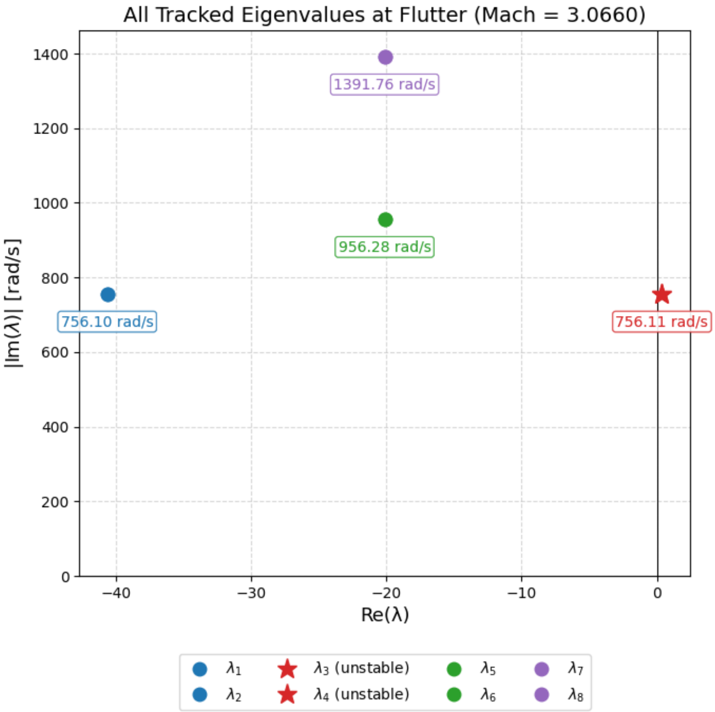

Source: Elaborated by the author.

It is also apparent from the frequency and eigenvalue evolution plots that, at the flutter condition, the first and second modes have nearly identical frequencies, although only the second mode becomes unstable. No evidence of instability was observed for the higher-order modes within the analyzed Mach number range.

6.3 Open-Circuit Conditions

In the open-circuit configuration, the shunt circuit presents a very high resistance ($R = 6 \cdot 10^6\ \Omega$), effectively imposing a no-displacement condition in the electrical domain ($D = 0$). As discussed in Section 2.1.4, this leads to an increase in the effective stiffness of the piezoelectric material, since the compliance is reduced by a factor of $(1 - k^2)$, theoretically making the piezoelectric material more resistant to deformation.

Figures 6 and 7 show the real and imaginary parts of the eigenvalues under this configuration. Flutter occurs at Ma = 2.969, which is slightly lower than in the short-circuit case. As seen in Figure 6, the real part of the eigenvalues associated with the second vibration mode becomes positive at this Mach number, signaling the onset of instability.

Figure 6 – Real part of eigenvalues under open-circuit conditions with modal tracking

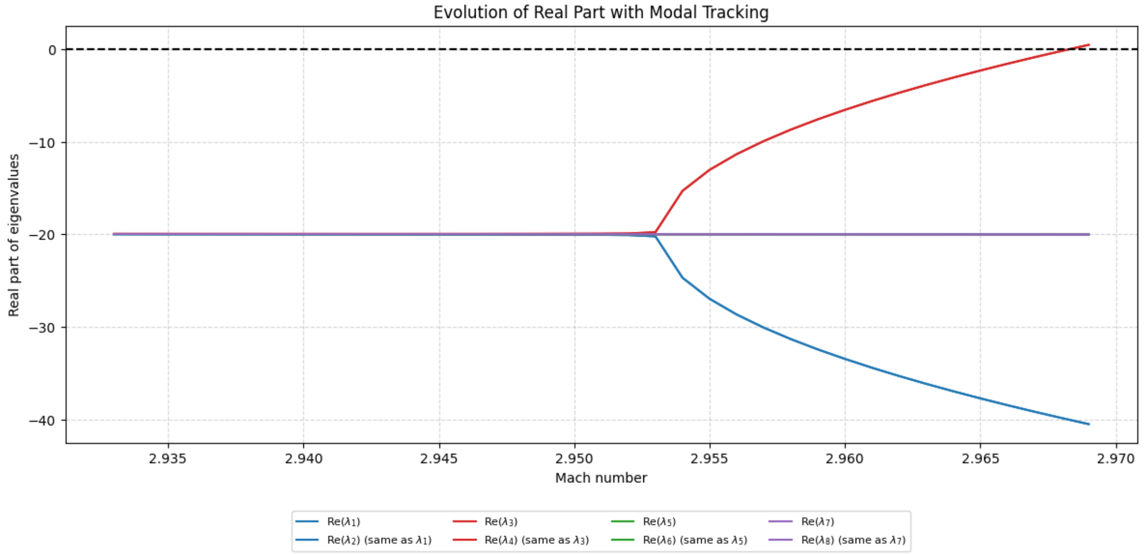

Source: Developed by the author.

The evolution of the real part of the eigenvalues is qualitatively similar to the short-circuit case, but the instability develops at a lower Mach number. Figure 7 shows the corresponding modal frequencies.

Figure 7 – Modal frequencies under open-circuit conditions

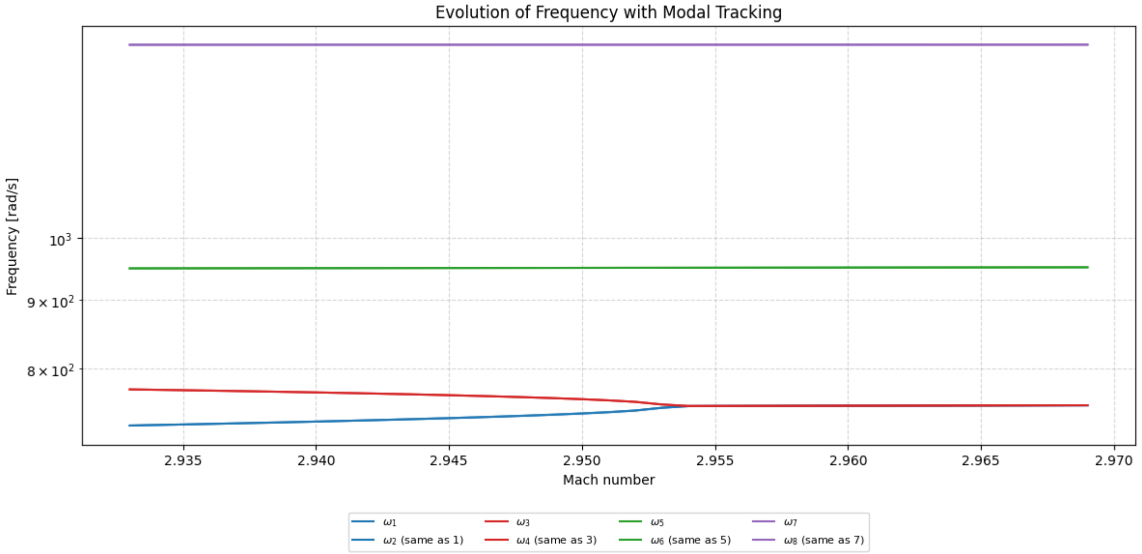

Source: Developed by the author.

Once again, the aeroelastic evolution displays a coalescence of the first and second modes, visible as their frequencies converge and become indistinguishable near the flutter boundary. This behavior is consistent with the classic flutter mechanism, where mode merging precedes instability. For clarity, the first four modes are shown in the complex plane at the flutter Mach number, as illustrated in Figure 8.

Figure 8 – First four modes of the system represented in the complex plane at the flutter Mach under open-circuit conditions

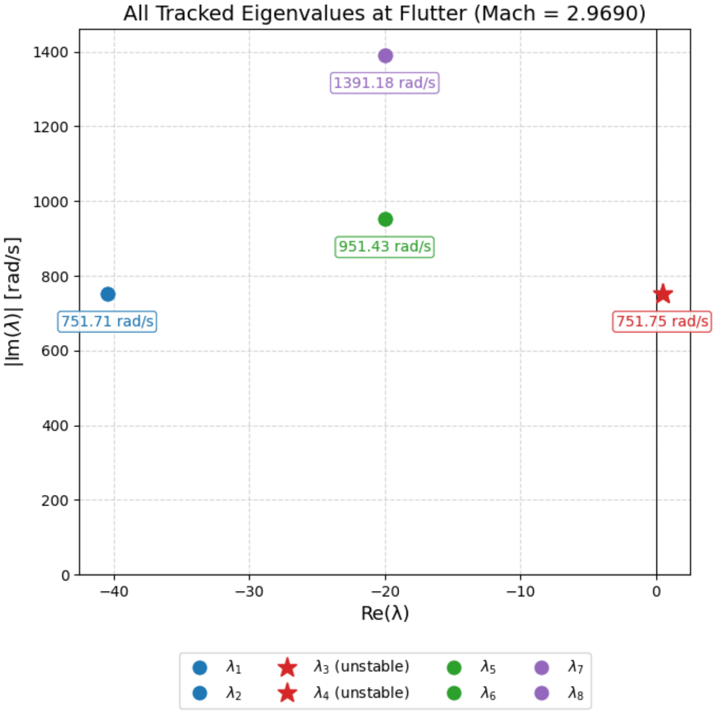

Source: Developed by the author.

It is noteworthy that, although the open-circuit configuration theoretically increases the structural stiffness of the piezoelectric sheets, it actually results in a lower critical Mach number for flutter compared to the short-circuit case. This seemingly counterintuitive outcome highlights that aeroelastic instability is not dictated by stiffness alone. The dynamic stability is influenced by a combination of modal energy distribution, electromechanical coupling, and the absence of dissipative mechanisms in the open-circuit scenario.

In the open-circuit case, the piezoelectric layers introduce reactive effects, but do not provide effective energy dissipation. This can lead to increased feedback into the structure and a reduction in the overall flutter margin. In contrast, the short-circuit case suppresses this feedback by imposing $E = 0$, decoupling the electrical and mechanical responses.

Thus, the earlier coalescence of modes and lower flutter Mach number observed in the open-circuit configuration can be attributed to the lack of dissipation and the unfavorable dynamic coupling, rather than to stiffness effects alone. This reinforces the importance of properly designed shunt circuits to enhance aeroelastic stability, which will be explored in the subsequent sections.

6.4 Preliminary Mapping of Flutter Behavior under Shunt Circuit Variation

In this subsection, the effect of varying resistance R and inductance L values in a passive shunt circuit connected to piezoelectric layers is explored. The goal is to evaluate how the electrical tuning influences the onset of aeroelastic instability.

Given that practical applications are limited by commercially available passive components, we restricted the analysis to the following ranges:

- $R \in [10^{-1}, 10^{4}]$ Ω, log-spaced over 9 values
- $L \in [10^{-2}, 10]$ H, also log-spaced over 9 values

This results in a grid of 81 circuit configurations. For each pair (R, L), a flutter analysis was performed using a coarse Mach number step of 0.1, starting at Ma $= 2.5$. The analysis stops as soon as the real part of the dominant eigenvalue becomes positive.

The resulting surface map of flutter Mach number is shown in Figure [9]. This topological representation highlights how circuit tuning can be used to delay or anticipate aeroelastic instability.

Figure 9 – Flutter Mach number as a function of $\log_{10}(R)$ and $\log_{10}(L)$ for the passive shunt circuit

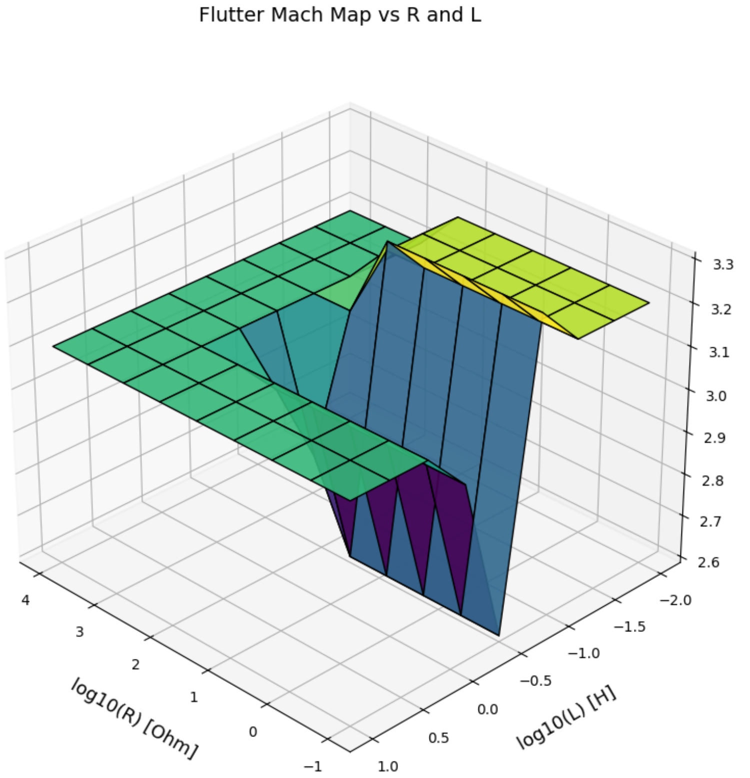

Source: Developed by the author.

The map reveals that the inductance L exerts a much more significant influence on the flutter boundary than the resistance R. This behavior indicates that dissipation alone—as governed by R—is insufficient to meaningfully alter the global aeroelastic response unless the circuit is also dynamically tuned. In particular, variations in reactance (linked to L) have a stronger impact on system stability, especially when approaching resonance with a structural mode.

This observation aligns with the well-established idea that passive shunt circuits must interact resonantly with the structural dynamics to be effective. When the circuit is far from such resonance, increasing resistance has little effect in delaying instability. The observed sensitivity to inductive tuning underscores the need to properly design circuit parameters based on the modal characteristics of the structure.

To reduce computational cost, this preliminary study was conducted with a coarse resolution in both the Mach sweep and the discretization of circuit elements. Nevertheless, the results successfully captured key trends and allowed identification of a promising configuration:

Maximum flutter Mach number found: $Ma = 3.3$
Achieved with: $R = 0.2371\ \Omega$, $L = 0.1778$ H

It is important to remember that the Mach step used is 0.1, so the true flutter Mach value may be up to 0.1 lower.

This result corresponds to a clear local maximum in the flutter Mach surface. While it may not represent the global optimum, it already provides a valuable indication of a promising operating region.

To refine the analysis, the next section will consider this configuration as a reference point. The goal will be to investigate whether it is possible to enhance damping by using the relations provided in Section 5.

6.5 Search for Optimized Shunt Parameters

After identifying a promising region in the (R, L) design space through a coarse parametric sweep, a local refinement was performed to more precisely assess the system's behavior near the best-performing configuration. The goals of this step are: (i) to confirm whether the selected point truly corresponds to a local maximum in flutter onset, and (ii) to accurately characterize the evolution of the dominant eigenmodes close to instability.

The Mach number was swept with a finer resolution (step size of 0.001), starting from $\mathrm{Ma} = 3.110$. Figures [10], [11], and [12] illustrate the evolution of the tracked eigenvalues and the precise Mach at which flutter occurs.

Figure 10 – Real part of eigenvalues near the optimal shunt configuration

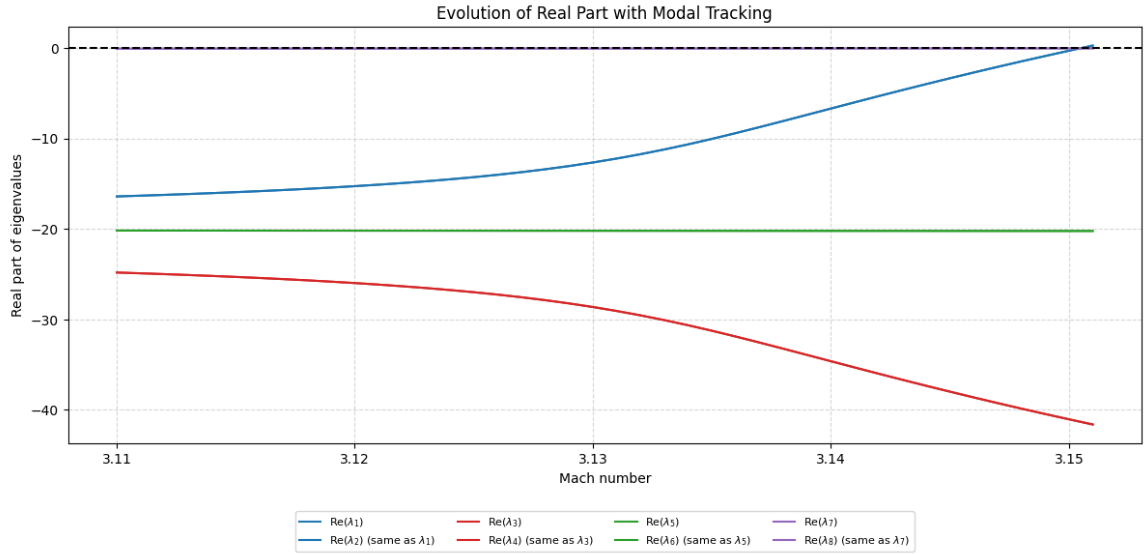

Source: Developed by the author.

As shown in Figure 10, flutter onset is observed at Ma = 3.151, where the real part of the first mode crosses zero and becomes positive. Prior to this point, all eigenvalues remain in the stable region with negative real parts. It is important to note, however, that the eigenvalues related to the fourth mode have a very small real part.

Compared to previous configurations, a noticeable separation emerges in the real parts of the lower modes, which were previously much closer together. This increased separation indicates enhanced modal damping as a result of the tuned shunt circuit. The corresponding modal frequencies are shown in Figure 11.

Figure 11 – Modal frequencies near the optimal shunt configuration

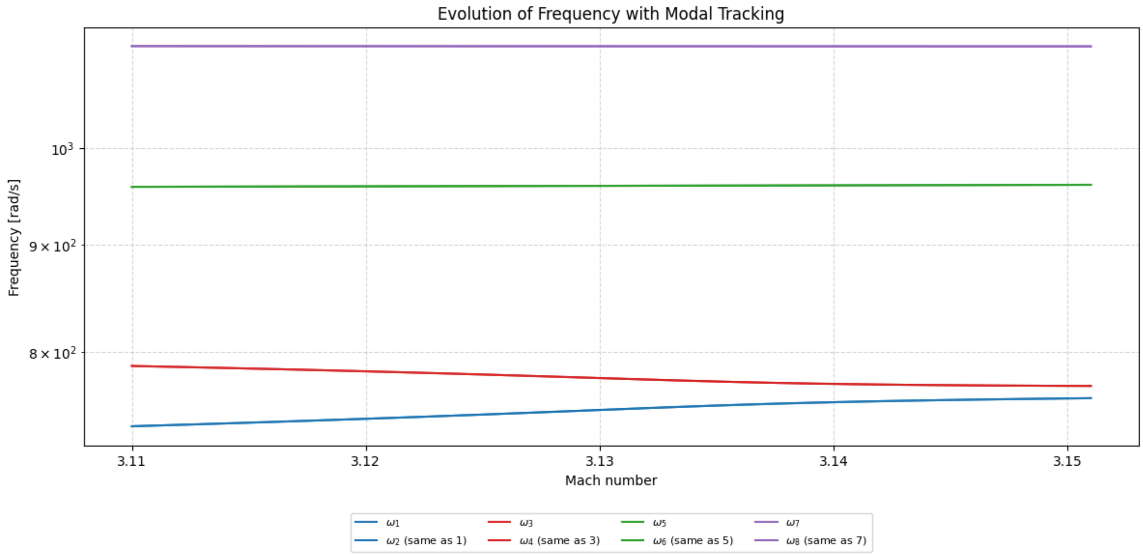

Source: Developed by the author.

Once again, we observe the coalescence of the first two modes, but their frequencies do not approach each other as closely as in previous cases; they do not merge before flutter occurs. This underscores the influence of the shunt circuit in modifying the system's modal frequencies and increasing the margin to instability. Figure [12] helps clarify this phenomenon, displaying the first four modes in the Argand-Gauss plane at the flutter condition.

Figure 12 – First four modes of the system represented in the complex plane at the flutter Mach for $R = 0.2371\ \Omega$, $L = 0.1778$ H

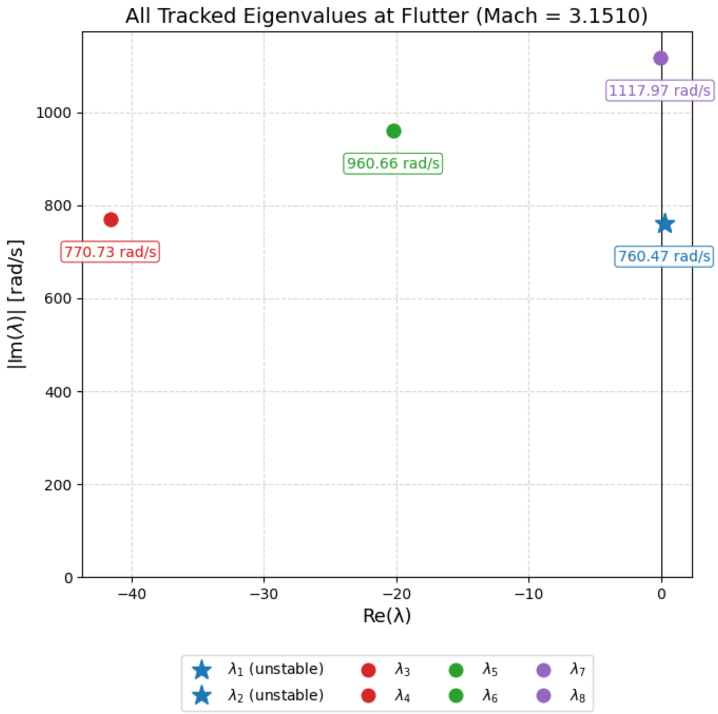

Source: Developed by the author.

In addition to the first mode, which is now located in the right half-plane (unstable), it is also evident that the fourth mode is marginally stable, with a very small negative real part ($\mathrm{Re}\{\lambda_{7,8}\} = -5.6929 \times 10^{-2}$). This suggests that the fourth mode is close to the stability boundary, but does not become unstable at this condition.

With this information, it is possible to pursue a more targeted tuning of the system. Building on the previous analysis, the next step is to refine the electrical parameters of the RL shunt circuit using the relations presented in Section 5.

Initially, using the data from the mode that becomes unstable (here, the first mode) appears to be the most logical choice for maximizing damping, as it tunes the shunt circuit to the frequency of the mode that first experiences flutter. However, applying Equation (5.1) with the obtained flutter frequency yields an inductance of $L = 0.4017\ H$, which quickly moves away from the local optimum indicated in Figure [9]. This reveals the limitation of relying solely on the most unstable mode, especially in coupled electromechanical systems.

Given this non-intuitive result, an alternative is to use the data from mode 4, as its real part is very close to zero (see Figure 12), indicating low damping and significant participation in the system's dynamic response. The calculated parameters are:

- Optimal inductance: $L_{\text{opt}} = 0.1859$ H
- Optimal resistance: $R_{\text{opt}} = 0.4742\ \Omega$ for $\zeta = 0.001$

Selecting a physically meaningful value of ζ (damping ratio) in coupled electromechanical systems is not straightforward. In this work, ζ was chosen by trial and error to balance flutter suppression and dynamic energy transfer. The chosen value, $\zeta = 0.001$, did not substantially affect the order of magnitude of the resistance. Notably, the values obtained for R and L are in the vicinity of the region highlighted as optimal in Figure 9.

After updating the shunt circuit with these refined values, the system response was re-evaluated using a new fine Mach sweep. The goal was to confirm whether the new parameters further delay flutter onset and thus enhance system stability. The results are shown in Figures 13, 14, and 15.

Figure 13 – Real part of eigenvalues with updated shunt circuit

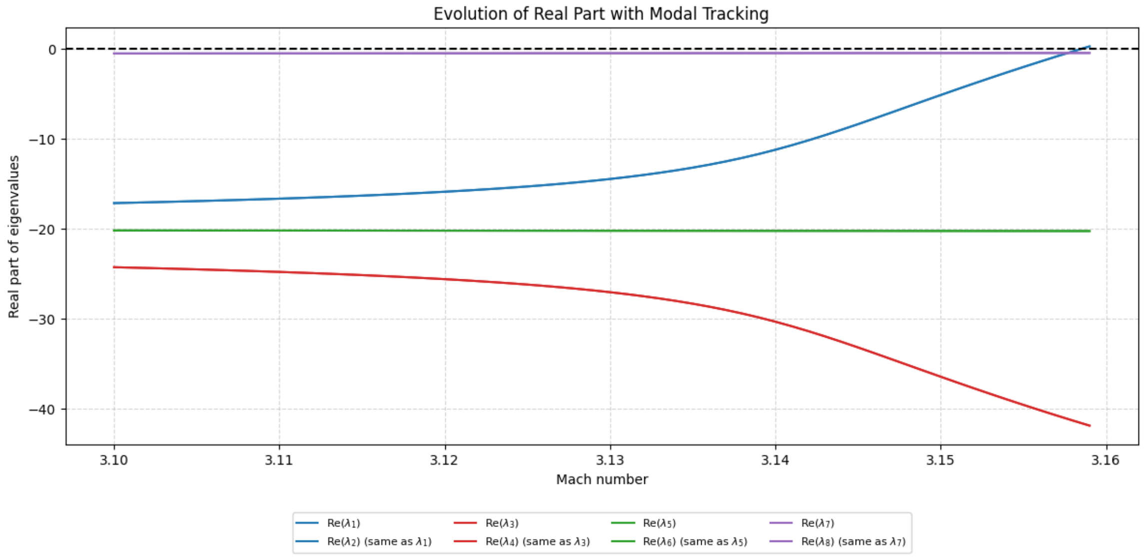

Source: Developed by the author.

Figure 13 demonstrates that flutter now occurs at Ma = 3.159, representing a modest but clear improvement compared to the previous configuration, which was at Ma = 3.151, and the same dominant eigenvalue (first mode) crosses the imaginary axis to become unstable.

Figure 14 – Modal frequencies with updated shunt circuit

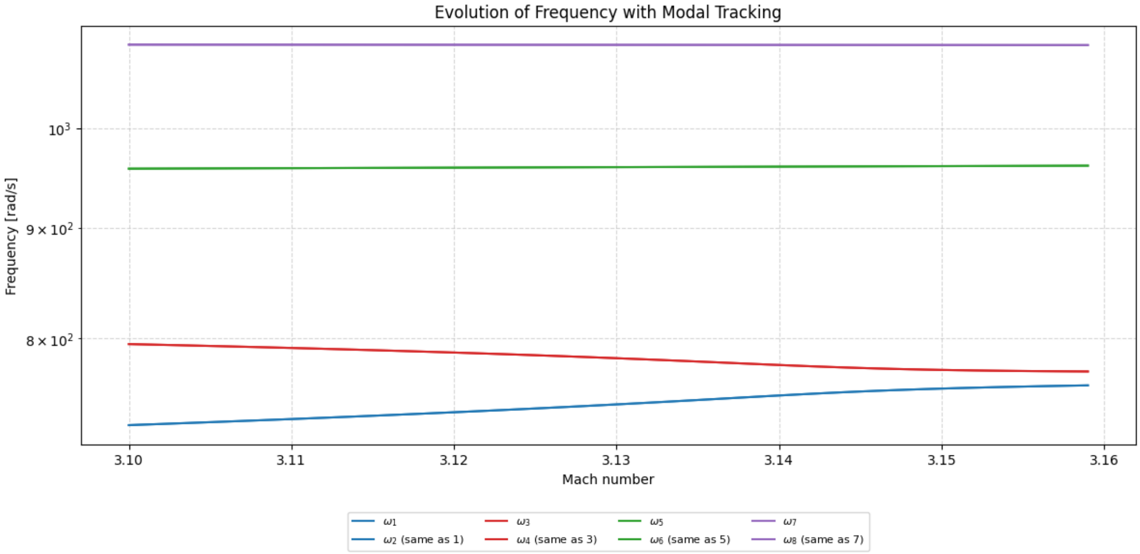

Source: Developed by the author.

Even though the first and second modes do not cross, Figure 14 shows the clear coalescence of their frequencies as Mach increases, a hallmark of the aeroelastic evolution to instability. Figure 15 depicts the final positions of the dominant modes in the complex plane at the flutter boundary.

Figure 15 – First four modes of the system represented in the complex plane at the flutter Mach for $R = 0.4156\ \Omega$, $L = 0.1859$ H

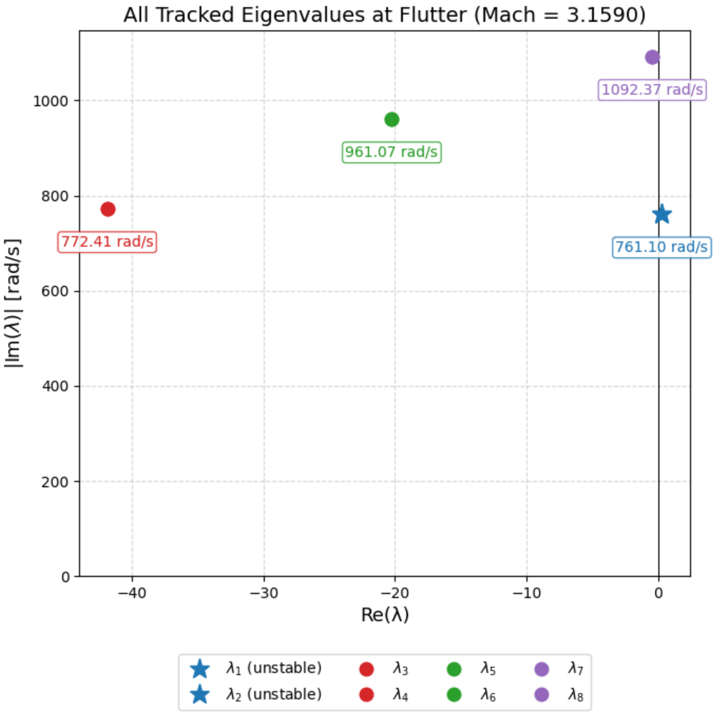

Source: Developed by the author.

These results confirm that fine-tuning the shunt circuit effectively increases the flutter margin, even if moderately. The critical Mach number rises by $\Delta\text{Ma} = 0.008$, highlighting the system's sensitivity to electrical boundary conditions and the efficacy of targeted electromechanical tuning.

Moreover, by tuning the shunt circuit to the fourth vibration mode, the module of its real part is increased, $\text{Re}\{\lambda_{7,8}\} = -4.2671 \times 10^{-1}$, compared to the previous configuration, indicating greater modal damping for this mode. This modification delays the onset of divergent aeroelastic phenomena, even though this mode is not the one that becomes unstable. Overall, the results reinforce the importance of targeted shunt tuning to maximize aeroelastic stability in piezoelectric-integrated structures.

6.6 Overall Comparison

Table 2 – Comparison of flutter results for different shunt circuit configurations

Case	**R** [Ω]	**L** [H]	$\mathbf{Ma}_{\text{flutter}}$	$\boldsymbol{\omega}_{\text{flutter}}$ [rad/s]	**Unstable Mode**
Open circuit (OC)	6×10^6	1×10^{-9}	2.969	751.75	2nd
Closed circuit (SC)	0	1×10^{-9}	3.066	756.11	2nd
First local maximum	0.2371	0.1778	3.151	760.47	1st
Optimized point	0.4156	0.1859	3.159	761.10	1st

Source: Developed by the author.

Table 2 reveals the main effects of electrical boundary conditions and shunt circuit tuning on flutter:

- **Non-monotonic stability:** The critical Mach number is not maximized by electrical stiffness alone; the open-circuit yields the lowest flutter margin, indicating that stability is driven by the interplay between stiffness, damping, and mode coupling.
- **Mode switching:** Instability shifts from the second mode (open and short-circuit) to the first mode in shunt-tuned cases, demonstrating strong electromechanical coupling and parameter sensitivity.
- **Shunt tuning effect:** RL shunt circuits, when tuned near optimal, raise the flutter Mach number and flutter frequency. Even moderate improvements confirm the practical impact of targeted passive damping.

In summary, optimized shunt circuits demonstrably enhance flutter margins in piezoelectric-integrated structures, but this benefit relies on careful tuning and understanding of the coupled dynamics.

7 CONCLUSION

This work presented the analysis of a numerical model for a piezoaeroelastic plate operating in supersonic flow, with piezoelectric layers connected to passive resistive-inductive (RL) shunt circuits. The formulation combined Kirchhoff–Love plate theory and Piston Theory to represent the aerody- namic forces, with Hamilton's principle applied to derive the coupled electromechanical equations of motion. A finite element framework was used to simulate modal behavior, capturing the structural deformation, aerodynamic loading, electromechanical coupling, and electrical energy dissipation.

The initial analyses compared flutter behavior under short-circuit and open-circuit electrical con- ditions. Notably, despite higher stiffness in the open-circuit configuration, flutter occurred at a lower Mach number (2.969) compared to the short-circuit case (3.066). This non-monotonic response demonstrates that increased stiffness alone does not guarantee improved aeroelastic stability. Instead, the interplay between electrical boundary conditions, energy dissipation, and modal interactions fundamentally governs the system's stability threshold. The results further revealed a shift in the critical instability mode: while flutter originated in the second mode for open- and short-circuit cases, it switched to the first mode for tuned shunt configurations, highlighting the strong mode coupling and the need for mode-resolved analysis.

To mitigate flutter, an RL shunt circuit was introduced and systematically tuned using parametric sweeps and frequency-matching strategies. The optimized configuration raised the flutter Mach number to 3.159, demonstrating the effectiveness of targeted passive damping. This enhancement, though moderate, was achieved by fine-tuning the circuit parameters and actively accounting for the coupled, nonlinear dynamics of the system. The results confirmed that passive shunt circuits can delay insta- bility not simply by increasing system stiffness, but by introducing modal damping and modifying the spectral properties at the flutter boundary.

A key limitation of the present study lies in the uniform coverage of the plate with piezoelectric material. While this simplifies modeling, it does not necessarily improve electromechanical coupling or damping efficiency, as demonstrated by Erturk et al. [5]. Only regions of high modal strain contribute meaningfully to energy conversion, and covering the entire surface may add unnecessary mass and even reduce effectiveness due to cancellation effects at strain nodes.

Future work should therefore focus on the optimal placement of piezoelectric patches, using modal strain energy distributions or topology optimization [14, 18]. Such strategies would enable more effective damping with less material, while further improvements could be achieved by extending the model to multi-modal coupling, adaptive circuits, or robust control approaches.

In summary, this study demonstrates the viability of passive piezoelectric damping for increasing the flutter margin in supersonic panels. The results underscore the importance of detailed, mode-resolved analysis and precise shunt tuning in harnessing the full potential of passive control. At the same time, the findings highlight the inherent nonlinearities and sensitivities of the coupled system, pointing to the need for advanced optimization strategies and practical design considerations in future applications.

References

[1] Holt Ashley and George Zartarian. Piston theory—a new aerodynamic tool for the aeroelastician. *Journal of the Aeronautical Sciences*, 23(12):1109–1118, 1956.

[2] S. Behrens, A. Fleming, and S. O. R. Moheimani. *A broadband controller for shunt piezoelectric damping of structural vibration*, volume 12. Smart Materials and Structures, 2003.

[3] Edward F Crawley and Jose de Luis. *Intelligent Material Systems and Structures: Active Materials: Volume 1.* Wiley, 1994.

[4] A. Dos Santos, V. Almeida, and L. S. Lopes. Passive vibration suppression using piezoelectric patches and rl shunt circuits: modeling and experimental validation. *Journal of Intelligent Material Systems and Structures*, 27(17):2317–2331, 2016.

[5] A. Erturk, P. A. Tarazaga, J. R. Farmer, and D. J. Inman. Effect of strain nodes and electrode configuration on piezoelectric energy harvesting from cantilevered beams. *Journal of Vibration and Acoustics*, 130(6):061008–1–061008–12, 2008.

[6] Alper Erturk and Daniel J. Inman. *Piezoelectric Energy Harvesting.* John Wiley & Sons, Chichester, UK, 2011.

[7] Nesbitt W. Hagood and Andreas von Flotow. Damping of structural vibrations with piezoelectric materials and passive electrical networks. *Journal of Sound and Vibration*, 146(2):243–268, 1991.

[8] Daniel J. Inman. *Engineering Analysis of Smart Material Systems.* John Wiley & Sons, 2007.

[9] Chong D. Lee. *Foundations of Adaptive Structures.* John Wiley & Sons, 2010.

[10] Donald J. Leo. *Engineering Analysis of Smart Material Systems.* John Wiley & Sons, Hoboken, NJ, 2007.

[11] Michael M. Liven. Analysis of piezoelectric shunting as a method of vibration control. *AIAA Journal*, 2(12):2235–2241, 1961.

[12] Dragan Marinković, Manfred Kessler, and Martin Hoffmann. A comprehensive model for piezoelectric energy harvesting using rl-shunted bimorphs. *Journal of Intelligent Material Systems and Structures*, 24(17):2095–2108, 2013.

[13] Dragan Marinković, Manfred Kessler, and Martin Hoffmann. A comprehensive model for piezoelectric energy harvesting using rl-shunted bimorphs. *Journal of Intelligent Material Systems and Structures*, 24(17):2095–2108, 2013.

[14] Chang Pan, Xiefei Zhang, and Wei Wang. A review of structural vibration control using piezoelectric materials. *Mechanical Systems and Signal Processing*, 143:106840, 2020.

[15] Singiresu S. Rao. *Vibration of Continuous Systems.* John Wiley & Sons, 2007.

[16] J. N. Reddy. *Theory of Plates and Shells.* CRC Press, 2007.

[17] S. Wang and W. Zhu. Energy harvesting from a piezoelectric laminate with a tuned inductive–resistive shunt. *Smart Materials and Structures*, 21(11):115011, 2012.

[18] Zhong Lin Wang and Jiayang Song. *Piezoelectric Vibration Energy Harvesting.* Springer Nature, 2022.

[19] J. Wu and Q. Wang. Piezoelectric damping of laminated composite plates with passive electrical networks. *Composite Structures*, 75(1–4):132–138, 2006.

[20] Wen Wu, Jun Wang, and Xiaodong Wang. Optimization of piezoelectric shunt damping for vibration control. *Smart Materials and Structures*, 20(4):045012, 2011.